International Journal of Solids and Structures 152–153 (2018) 228–237

Contents lists available at ScienceDirect

International Journal of Solids and Structures

journal homepage: www.elsevier.com/locate/ijsolstr

# Frequency-dependent cohesive-zone model for fatigue

S. Salih[a,b,*], K. Davey[a], Z. Zou[a]

[a] School of Mechanical, Aerospace and Civil Engineering, The University of Manchester, Manchester, United Kingdom
[b] School of Engineering, The University of Babylon, Hillah, Iraq

ARTICLE INFO

*Article history:*
Received 15 August 2017
Revised 1 May 2018
Available online 30 June 2018

*Keywords:*
Fatigue crack growth
Cohesive zone model
Frequency dependence
Computational efficiency

ABSTRACT

This paper is concerned with the development and application of a frequency-dependent cohesive-zone model (CZM) for crack-growth analysis of low and high-cycle fatigue. The new model makes use of recent advances by combining a modified version of a recently developed frequency-dependent trapezoidal cohesive-zone model (Salih et al., 2017) and a new *loading-unloading hysteresis damage model* with *fast-track* facility. The new combined model offers an alternative approach to capture frequency effects and at the same time deliver accuracy comparable to the *loading-unloading hysteresis damage model* along with the computational efficiency of the equally well-established *envelope load-damage model*. The model provides for the first time a methodology that accommodates frequency dependency yet delivers high computational efficiency.

In order to demonstrate the practical worth of the approach, the frequency effect observed with fatigue crack growth in austenitic stainless-steel 304 is analysed. It is found that the crack growth decreases with increasing frequency up to a frequency of 5 Hz after which it levels off. The behaviour, which can be linked to martensitic phase transformation, is shown to be accurately captured by the new model.



## 1. Introduction

Austenitic stainless-steel 304 is widely used in many structural and mechanical applications common to automotive industries and power plants, where toughness and resistance to corrosion are required (Colin et al., 2010). The austenite phase in this stainless-steel is unstable and easily transforms to martensite under plastic deformation. Although, this feature makes this type of stainless-steel a good candidate for many applications, it is important to appreciate that for cyclic-loading applications the rate at which fatigue cracks grow can vary significantly with the applied load frequency.

The strength of the austenitic stainless-steel is affected by the martensitic content. Martensite formation depends on the strain amplitude, temperature, grain size and the number of loading cycles (Ganesh Sundara Ranan and Padmanabhan, 1995; Ye et al., 2006). The dependence on strain amplitude means that the austenitic-martensitic phase transformation is significantly more sensitive in this regard to low-cycle fatigue (LCF) as opposed to high-cycle fatigue (Ye et al., 2006; Baudry and Pineau, 1977). However, the transformation can occur with high-cycle fatigue (HCF) as a result of plastic-strain accumulation (Colin et al., 2010; Lebedev and Kosarchuk, 2000). The percentage of martensite in this case however tends to be small, and typically no greater than 3% according to reference (Müller-Bollenhagen et al., 2010). Further details on the effects of plastic-strain amplitude, temperature and chemical composition on the formation of the strain-induced martensite is available in references (Ye et al., 2006; Lebedev and Kosarchuk, 2000).

As the austenitic-martensitic phase transformation depends on the plastic deformation, which in turn is dependent on strain rate, it follows that the frequency at which the cyclic load is applied can have an effect on the martensitic content and consequentially on fatigue crack-growth rates. Although, the meta-stable austenitic stainless-steel type 304 is widely used in many applications, there is limited work on the effect of frequency on the fatigue crack growth in this material. Exceptions are references (James, 1972) and (Nikitin and Besel, 2008), where the influence of temperature is discussed.

The effect that the frequency has on fatigue crack growth in austenitic stainless-steel 304 under sinusoidal cyclic load with stress ratios ($R=0$ and $R=-1$) and a maximum load of 10 KN applied in a standard environment at room temperature is investigated as part of this study. However, fatigue experimentation is both time consuming and costly, so coupling this to a numerical model that can capture frequency effects is of some im-

*Abbreviation:* CE, Cohesive element; CZM, Cohesive-zone model; TCZM, Trapezoidal cohesive-zone model.

* Corresponding author.
*E-mail addresses:* sarmed.salih@manchester.ac.uk (S. Salih), keith.davey@manchester.ac.uk (K. Davey), zhenmin.zou@manchester.ac.uk (Z. Zou).

https://doi.org/10.1016/j.ijsolstr.2018.06.030
0020-7683/

**Nomenclature**

*List of symbols*

| | |
|---|---|
| $D^c$ | Cyclic damage |
| $D^s_{(\delta)}$ | Static damage |
| $D$ | Total damage |
| $E$ | Elastic modulus |
| $K_{coh}$ | Cohesive stiffness |
| $G_c$ | Total dissipated energy per unit area |
| $G^p$ | Dissipated plastic energy in the cohesive-zone per unit area |
| $N$ | Number of cycles |
| $\Delta N$ | Number of cycles in the load envelope |
| $N_u$ | Number of required damage updates |
| $\delta_c$ | Critical separation |
| $\delta_1$ | Shape parameter for the linear and trapezoidal model respectively |
| $\delta_2$ | Second shape parameter of the trapezoidal model |
| $\delta^p$ | Plastic separation |
| $\delta^p_{(N)}$ | Plastic separation after $N$ number of cycles |
| $\delta^{cyc}$ | Cyclic displacement |
| $\delta^{cyc(max)}_{(N)}$ | Maximum displacement reached at a loading cycle |
| $\delta$ | Applied separation (plastic separation plus the cyclic displacement) |
| $\delta_{max}$ | The separation at the onset of unloading |
| $\sigma_c$ | Critical cohesive stress |
| $\sigma^{crate}_{(f)}$ | Frequency-dependent critical cohesive stress |
| $\sigma$ | Cohesive stress |
| $\sigma_Y$ | Yield stress |
| $\sigma_{max}$ | The stress at the onset of unloading |
| $\Gamma_o$ | Critical cohesive energy |
| $\vartheta$ | Poisson's ratio |

portance. The academic literature reveals that the cohesive-zone model (CZM) is an attractive candidate for the modelling and simulation of fatigue problems. The vast majority of CZMs discussed in the literature however are limited to monotonic crack propagation. To use the CZM for fatigue analysis, it is required to accommodate cyclic damage accumulation within the traction separation law. There are two principal approaches reported in the literature for identifying cyclic-damage formulation; these are the *loading-unloading hysteresis damage model* and the *envelope load-damage model*.

In the *envelope load damage model*, the maximum load of the loading cycle is of principal interest rather than the complete cyclic-loading behaviour. All variants founded on this particular approach formulate a relationship for damage rate $dD/dN$, which for convenience is written here symbolically in the form of a derivative despite $D$ being a path-dependent quantity. The damage $D$ is assumed to take the additive form $D = D_s + D_c$, where $D_c$ is a cyclic damage component and $D_s$ is a monotonic damage component. A full review of the different formulations for the cyclic-damage rate that adopted in the literature can be found in reference (B.L.V. Bak et al., 2014).

On the other hand, in the *loading-unloading hysteresis damage models*, the entire loading-unloading cycle is considered and represented. This feature permits the modelling of complicated behaviour (such as friction and plasticity) at the cohesive interface and the crack tip surroundings (B.L.V. Bak et al., 2014). The first *loading-unloading hysteresis damage models* was introduced by De-Andrés et al. (1999) for fatigue crack growth simulation. In this model, a cyclic damage factor $D$ is proposed to quantify the amount of dissipated energy in the fracture process after a specific number of cycles divided by the critical cohesive energy. This work was soon followed with the introduction of variable-interfacial stiffness models; see for example Nguyen and Repetto (2001) and Yang et al. (2001), where traction rate $\dot{T}$ is assumed to be a function of incremental stiffness $K_{(\delta)}$ and separation rate $\dot{\delta}$, i.e. explicitly $\dot{T} = K_{(\delta)}\dot{\delta}$. A more sophisticated model is presented in reference (Roe and Siegmund, 2003), where two additional parameters $\delta_\Sigma$ and $\sigma_f$ represent the accumulated cohesive length and the fatigue limit, respectively. If the cohesive traction evaluated by the model at the crack tip is less than $\sigma_f$, then the model returns an infinite life (no crack will propagate). Similar approaches have been considered in references (Ural et al., 2009; Beaurepaire and Schuëller, 2011).

Although, fatigue behaviour is replicated reasonably well by the *loading-unloading hysteresis damage model*, the approach from a practical viewpoint is considered rather costly in terms of the required computational time. In particular it is considered unfeasible for the simulation of high-cycle fatigue, which can typically involve extremely large numbers of loading cycles. Although attempts to reduce the cost associated with hysteresis-damage models are considered in references (De-Andrés et al., 1999; Towashiraporn et al., 2005; Koutsourelakis et al., 2006), by involving extrapolation, these models suffer severe accuracy limitations.

An extrapolation scheme to *fast-track* the crack growth rate has recently been developed by the authors of this work for speeding up the *loading-unloading hysteresis damage model* (Salih et al.), although frequency dependence is not considered. The proposed new loading-unloading hysteresis damage model with the fast-track facility is further extended in this paper to accommodate frequency-dependent behaviour. The new frequency-dependent CZM is discussed in Section 2. Included there is information on the loading-unloading hysteresis damage model and a brief description on the fast-track capability. The mathematical model is encoded into a UMAT subroutine for implementation in the commercial finite element package ABAQUS; details on this are presented in Section 3. Section 4 focuses on investigating crack growth in stainless steel 304 experimentally and numerically; this includes details about the analysis model (geometry, material properties, and boundary conditions) along with mesh sensitivity analysis and the validation of the new model. Conclusions are presented in Section 5.

## 2. Cohesive-zone model

### 2.1. Loading-unloading hysteresis damage CZM with fast-track feature

If cyclic load is applied to a standard CZM, the outcome is an infinite life. In order to capture a finite life, it is necessary to identify a cyclic damage accumulation mechanism within the cohesive model. This damage will monotonically increase with the number of cycles leading to the failure of the cohesive element. The proposed cohesive model for fatigue is described mathematically as

$$\sigma_{(\delta)} = \begin{cases} K_{coh}\delta & \text{if } \delta < 0 \\ \left(\frac{\sigma_{max}}{\delta_{max}-\delta^p}\right)(\delta-\delta^p)H(\delta-\delta^p) & \text{if } 0 \le \delta \le \delta_{max} \\ \left(1-D^s_{(\delta)}\right)K_{coh}\delta & \text{if } \delta_{max} < \delta < \delta_c \\ 0 & \text{if } \delta \ge \delta_c \end{cases} \quad (1)$$

where $K_{coh}$ represents the cohesive stiffness, $\sigma_{(\delta)}$, $\sigma_c$, $\sigma_{max}$ and $\delta_{max}$ are the cohesive traction, the critical cohesive stress, the stress and the separation at the point of unloading, respectively (see Fig. 1). In the figure, $\sigma_{\max(1)}$ and $\delta_{\max(1)}$ are the value of the maximum stress and separation after the first loading cycle and accordingly $\sigma_{\max(2)}$ and $\delta_{\max(2)}$ after the second loading cycle. To ensure that the first part of the second relationship of Eq. (1) ( i.e. $\sigma_{max}/(\delta_{max}-\delta^p)$) returns the cohesive stiffness $K_{coh}$

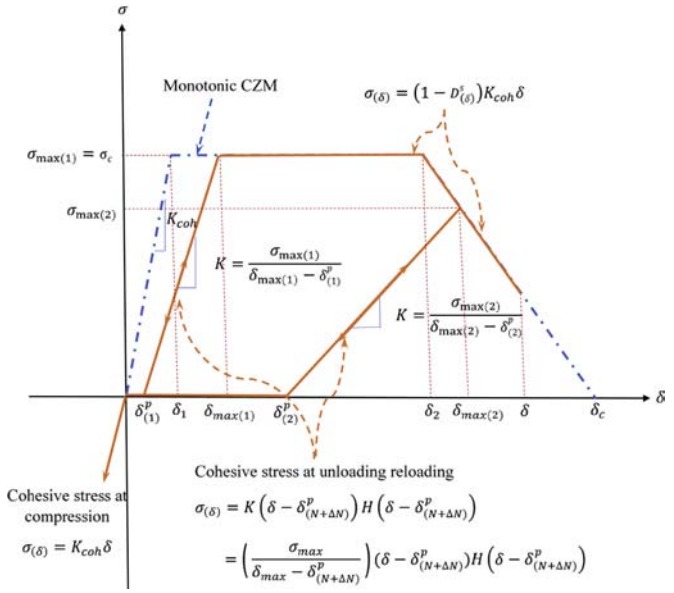


**Fig. 1.** The loading-unloading representation of the CZM.

when there is no damage at $\delta \leq \delta_1$ *and* $\delta^p = 0$ the value of $\sigma_{max}$ and $\delta_{max}$ are set to be equal to $\sigma_c$ and $\delta_1$, respectively. Here $\delta_c$, $\delta_1$, $\delta_2$, $\delta$ and $\delta^p$ are the critical cohesive separation, the separation at which the permanent damage starts, the separation at which the material deterioration starts, the applied separation and the remnant separation after unloading, respectively. The Heaviside function $H(\delta - \delta^p)$ in Eq. (1) is defined to equal zero if $\delta$ is smaller than $\delta^p$ and one in any other condition. Finally, $D^s_{(\delta)}$ is a monotonic damage variable.

The damage mechanism adopted in this model consists of two parts: a cyclic damage $D^c$ and a monotonic damage $D^s_{(\delta)}$. The cyclic damage $D^c$ is a result of the accumulation of plastic deformation and is a consequence of two different effects: (i) cyclic plasticity build-up, represented by the increase in cyclic plastic deformation $\delta^p$ when the separation $\delta \leq \delta_2$ and; (ii) a further increase in $\delta^p$ as a result of the void growth and coalescence when $\delta > \delta_2$. The monotonic damage $D^s_{(\delta)}$ is a result of material deterioration of the non-cyclic variety, $D^c$ and $D^s_{(\delta)}$ combine additively to give the total damage, i.e.

$$D = D^c + D^s_{(\delta)} \tag{2}$$

The monotonic damage variable $D^s_{(\delta)}$ is evaluated from

$$D^s_{(\delta)} = \begin{cases} 1 - \dfrac{\delta_1}{\delta} & \text{if } \delta_1 \leq \delta < \delta_2 \\ 1 - \dfrac{\delta_1(\delta_c - \delta)}{\delta(\delta_c - \delta_2)} & \text{if } \delta_2 \leq \delta \leq \delta_c \end{cases} \tag{3}$$

The choice of $\delta_1$ and $\delta_2$ is arbitrary (since there are no evidence of the right shape of the traction-separation law). The value of $\delta_1$ is set to a relatively small value to ensure a very stiff connection in the undamaged cohesive elements, while $\delta_2$ is set to be close to $\delta_c$ to capture the local dissipated energy at the crack tip as a result of local plastic deformation, since the focus of the model is crack propagation in ductile materials. These choices is similar to what is advised in reference (Scheider et al., 2006), for definiteness $\delta_1$ and $\delta_2$ are set as

$$\delta_1 = \frac{\sigma_c}{K_{coh}} \tag{4}$$

$$\delta_2 = 0.75 \times \delta_c \tag{5}$$

The applied separation $\delta$ is determined by adding the applied cyclic displacement $\delta^{cyc}$ to the remnant separation $\delta^p$, i.e.

$$\delta = \delta^p + \delta^{cyc} \tag{6}$$

The plastic remnant $\delta^p$ is updated by adding the result of integrating the cyclic-plasticity rate $(d\delta^p_{(N)}/dN)$ to its value from the previous plastic separation, i.e.

$$\delta^p_{(N+\Delta N)} = \delta^p_{(N)} + \int_N^{N+\Delta N} \left(d\delta^p_{(N)}/dN\right)dN' \tag{7}$$

where $N$ is the number of cycles, $\Delta N$ is the number of cycles between updates in the damage state, $\delta^p_{(N+\Delta N)}$ is the updated plastic separation, $\delta^p_{(N)}$ is the previous plastic separation, and $d\delta^p_{(N)}/dN$ is the cyclic-plasticity rate (the derivative format is used here for convenience).

The mean value theorem for integration is used to approximate the integral in Eq. (7), where $d\delta^p_{(N)}/dN$ is assumed to be defined and smooth on the interval $(N, N+\Delta N)$. Integration provides

$$\int_N^{N+\Delta N} (d\delta^p_{(N)}/dN)dN' = \left(d\delta^p_{(N)}/dN\right)_{(\alpha)} \times \Delta N \tag{8}$$

where $\alpha$ is a value that belongs to the interval $[N, N+\Delta N]$ and $(d\delta^p_{(N)}/dN)_{(\alpha)}$ is an intermediate value of the rate $d\delta^p_{(N)}/dN$.

A suitable approximation for $(d\delta^p_{(N)}/dN)_{(\alpha)}$ is

$$\left(d\delta^p_{(N)}/dN\right)_{(\alpha)} \approx \frac{\delta^{cyc_{(max)}}_{(N)}}{C} \tag{9}$$

where $C$ is a material parameter greater than unity and $\delta^{cyc_{(max)}}_{(N)}$ is the maximum displacement reached at the end of a loading cycle.

The choice for the approximation of Eq. (9) is expedient since it relates the change in the cyclic plasticity to the loading conditions through $\delta^{cyc_{(max)}}_{(N)}$ with the ability to capture any material cyclic behaviour through the material parameter $C$, which can be tuned by comparing the numerical results with the experimental data to accommodate the cyclic behaviour of a particular material. Substitution of Eq. (9) into Eq. (7) yields an extremely simple cyclic-plasticity incremental rule, i.e.

$$\delta^p_{(N+\Delta N)} \approx \delta^p_{(N)} + \frac{\delta^{cyc_{(max)}}_{(N)}}{C}\Delta N \tag{10}$$

For the conventional loading-unloading hysteresis damage model $\Delta N$ is equal to 1. However, if the extrapolation scheme is applied to fast-track the crack propagation, the increment $\Delta N$ is set to have an integer value significantly greater than one for computational practicality (Salih et al.). Although, the value of $\Delta N$ can affect the accuracy of the result, an acceptable estimation of $\Delta N$ can be evaluated at the first integration point at the crack tip for the specified loading conditions by running a one cycle analysis and apply the following relationship

$$\Delta N = int\left(\frac{\delta_c - \delta^{cyc_{(max)}}_{(1)}}{N_u \times \delta^p_{(1)}}\right) \tag{11}$$

where *int* is a function that returns the nearest integer to the argument, $\delta^p_{(1)}$ and $\delta^{cyc_{(max)}}_{(1)}$ are the cyclic plasticity after the first loading cycle and the maximum cyclic displacement reached at the first loading cycle, respectively. The parameter $N_u$ represents the number of required updates of the cyclic damage.

For simplicity $\Delta N$ is assumed to be invariant for the whole process and at the end of the $N+\Delta N$ cycles $\delta_{max}$ and $\sigma_{max}$ are determined with

$$\delta_{max} = \delta^p_{(N+\Delta N)} + \delta^{cyc_{(max)}}_{(N)} \tag{12}$$

and

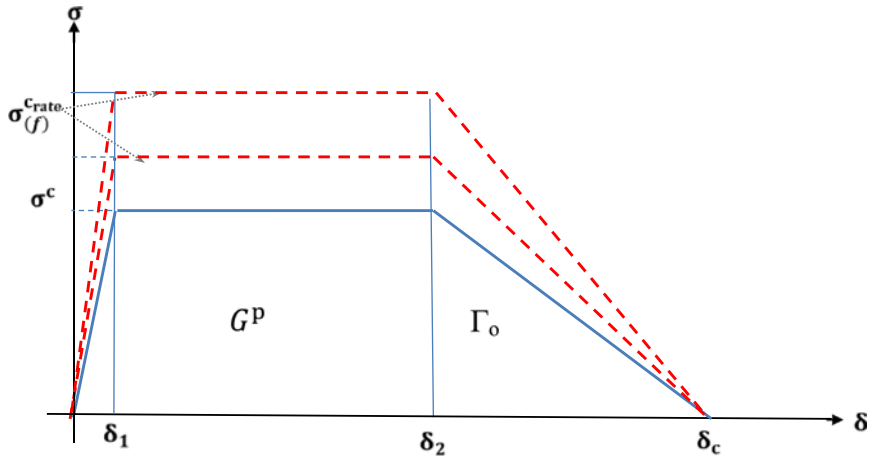


**Fig. 2.** Mode I Trapezoidal frequency-dependent CZM.

$$\sigma_{max} = \begin{cases} \sigma_c & \text{if } \delta_1 < \delta_{max} \le \delta_2 \\ \left(1 - D^s_{(\delta_{max})}\right) \times \sigma_c & \text{if } \delta_2 < \delta_{max} \le \delta_c \end{cases} \tag{13}$$

where $D^s_{(\delta_{max})}$ is the static damage of Eq. (3) with $\delta$ replaced by $\delta_{max}$ evaluated from Eq. (12).

The accumulated dissipated energy ($\Delta G$) at the end of any loading cycle is given by

$$\Delta G = \begin{cases} \frac{1}{2}[\sigma_c(\delta_{max} + \delta^p - \delta_1)] & \text{if } \delta_{max} \le \delta_2 \\ \frac{1}{2}[\sigma_c(\delta_{max} + \delta_2 - \delta_1) - \sigma_{max}(\delta_2 - \delta^p)] & \text{if } \delta_{max} > \delta_2 \end{cases} \tag{14}$$

The calculated values of $\delta_{max}$ and $\sigma_{max}$ from Eqs. (12) and (13) along with the updated separation $\delta$ from Eq. (6) are applied in Eq. (1) at the next loading cycle.

The number of cycles is updated after the end of a loading cycle through the relationship $N_{i+1} = N_i + \Delta N$. However, if the separation in the cohesive element reaches the critical cohesive separation in a number of cycles less than $N_{i+1}$, then the exact number of cycles at which the cohesive element failed satisfies the relationship

$$N_f = N_{i+1} - int\left(\frac{\delta_{max} - \delta_c}{\delta^{cyc_{(max)}}_{(N)}/c}\right) \tag{15}$$

which is important for the determination of an accurate crack length-number of cycles curves.

### 2.2. Frequency-dependent CZM for fatigue

To produce a frequency-dependent CZM that can be used for the analysis of high and low-cycle fatigue, it is necessary to link the fatigue model introduced in Section 2.1 with a frequency-dependent critical stress, the TCZM with the frequency-dependent critical stress is shown is Fig. 2. The same concept of the rate-dependent cohesive model with critical stress limit introduced in reference (Salih et al., 2016) is adopted here to produce an empirical formula for the frequency-dependent critical stress ($\sigma^{c_{rate}}_{(f)}$). The stress $\sigma^{c_{rate}}_{(f)}$ increases with the frequency up to a specific limit $\sigma^{c}_{(limit)}$ and is assumed to behave exponentially and is represented mathematically by

$$\sigma^{c_{rate}}_{(f)} = \sigma^{c}_{(limit)} \times exp\left(-\frac{f_o}{f}\right) \tag{16}$$

where $\sigma^{c}_{(limit)}$ is the maximum value for the increase in the frequency-dependent critical stress, its value evaluated from tuning with the experimental data at loading frequency of 50 Hz. The value of the base frequency $f_o$ is set to ensure that at 0.05 Hz the frequency-dependent critical stress equals the yield stress at a proof strain equal to 0.1%. Note also that Eq. (16) arises out of a rheological model satisfying the differential equation $d\sigma^{c_{rate}}_{(f)}/d\tau = -\sigma^{c_{rate}}_{(f)}$, where $\tau$ represents a dimensionless time and for frequency loading is related to frequency by $\tau = f_0/f$. Although the particular form of Eq. (16) is not unique it provides a relatively simple model for the desired response of $\sigma^{c_{rate}}_{(f)}$. Note that as $f \to \infty$ the function $\sigma^{c_{rate}}_{(f)}$ asymptotically approaches the constant value $\sigma^{c}_{(limit)}$, which is an effect observed experimentally as discussed in reference (Salih et al., 2016). This behaviour arises from the saturation of fracture energy with rate and for austenitic stainless-steel 304 it can be linked to the saturation of the austenitic-martensitic phase transformation. In essence the frequency-dependent fatigue model consists of the model outlined in Section 2.1 apart from $\sigma^{c_{rate}}_{(f)}$ replacing $\sigma_c$. This is illustrated graphically in Fig. 1 and described mathematically by Eq. (1).

## 3. Implementation of the new cohesive-zone model in ABAQUS

In this study, the commercial finite element solver ABAQUS (ABAQUS 2013) is chosen to be the vehicle for performing the numerical analysis. In ABAQUS, the cohesive model can be identified either in the form of cohesive surface or by implementing cohesive elements in the numerical model along the crack path. Introducing a new cohesive model to ABAQUS is achieved with the cohesive element through a user-defined material (UMAT) subroutine.

### 3.1. Implementation and testing of the new CZM

The new frequency-dependent CZM is implemented in ABAQUS by using a UMAT subroutine. To test the subroutine and to demonstrate the benefit of using the fast-track feature, a three-element model (3-EM) (two material elements linked through a cohesive element) is initially used as shown in Fig. 3. Shown in Table 1 are the properties of the bulk material element and the cohesive element. The boundary conditions are displacement fixed in all directions at the bottom edge and a constant cyclic displacement applied at three loading frequencies (0.05, 0.1 and 30 Hz) with $R = 0$ and 7.3 mm maximum amplitude at the top edge (see Fig. 3). Figs. 4 to 6 shows the cyclic stress with the real time at different loading frequencies. From these curves, the behaviour of the new

**Table 1**
Stainless-steel 304 Material and cohesive properties.

| Bulk material | Young's modulus ($E$) (GPa) | | | Poisson's ratio ($\vartheta$) | | |
|---|---|---|---|---|---|---|
| | 193 | | | 0.29 | | |
| Cohesive elements | $G_c$ (N/m) | $K_{coh}$ (GPa/m) | $\sigma_c$ (MPa) | $\delta_c$ (m) | $\delta_1$ (m) | $\delta_2$ (m) |
| | ,470,39 | 19,700 | 340 | 0.000168 | 0.0000173 | 0.000126 |
| | $\Delta N$ | | $\sigma^c_{(limit)}$ (MPa) | $f_o$ (Hz) | C 3-EM | C Full-model |
| | 1 | 4 | 400 | 0.008 | 40 | 775 |

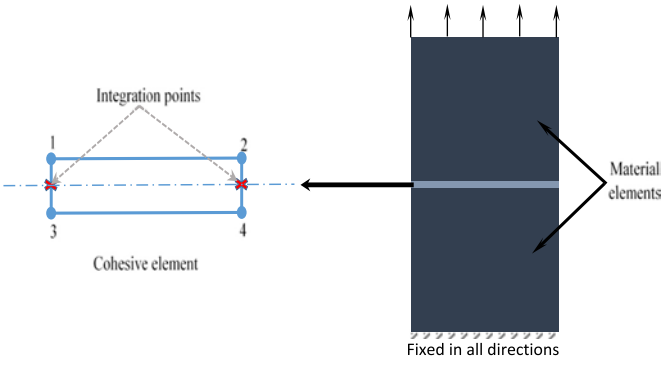


**Fig. 3.** Implementation of the cohesive element in the finite element model.

frequency-dependent model is illustrated. Increasing the frequency increases the critical stress of the cohesive model and at the same time the advantage of the fast-track feature is illustrated by comparing the number of cycles required to finish the analysis (both analyses involve real fatigue cycles of about 26 cycles). Application of the fast-track feature provides a reduction in CPU-time of the order of $\Delta N^{-1}$.

## 4. Experimental and numerical study on fatigue crack growth in stainless steel 304

### 4.1. Experimental study

The effect of frequency on fatigue crack growth has been investigated experimentally on the austenitic Stainless-steel type 304.

**Table 2**
Chemical composition (wt. %).

| C | Si | Mn | Ni | Cr | N | S | P |
|---|---|---|---|---|---|---|---|
| 0.021 | 0.35 | 1.48 | 8.03 | 18.13 | 0.072 | 0.004 | 0.033 |

This material is recognized to be sensitive to strain rate, suffering a strain-induced phase transformation, making it a good candidate for testing out the new fatigue model.

#### 4.1.1. Material properties

The meta-stable austenitic stainless-steel (AISI type 304) used in this study has the material composition and mechanical properties tabulated in Tables 2 and 3, respectively.

#### 4.1.2. Specimen preparation

An electrical discharge machine (EDM) was used to cut the specimens from a rectangular cross section stainless-steel bar with dimensions $0.003 \times 0.04 \times 4$ m. The shape and dimensions of the Fatigue specimens are shown in Fig. 7. The specimens were finished by using different wet silicon carbide papers (320, 600, 1200, 2500, and 4000) and then polished with diamond solution (9 µm). After polishing, a stress relieving process (heating to $400 \pm 5$ °C for 20 minutes and left to cool in an oven) has been performed to remove any residual stresses. The specimens were subsequently polished with diamond solution (6 µm) to remove any oxide and to achieve a very fine surface finish.

Fatigue tests were performed using an Instron 8801 servo-hydraulic fatigue testing machine rated with a maximum load capacity of 100 kN. Six loading frequencies with a loading ratio $R = 0$ {50, 30, 5, 0.5 0.1, 0.05 Hz} and three with $R = -1$ {30, 0.1,

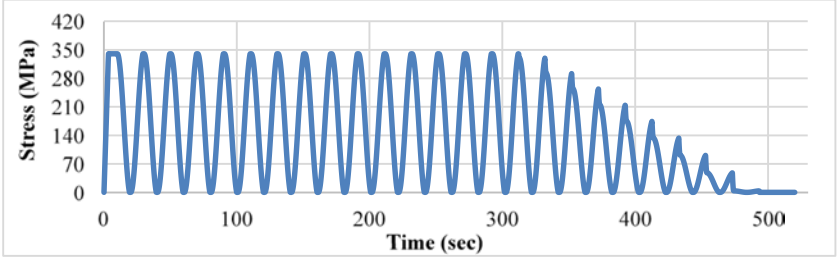


(a) cycle by cycle analysis

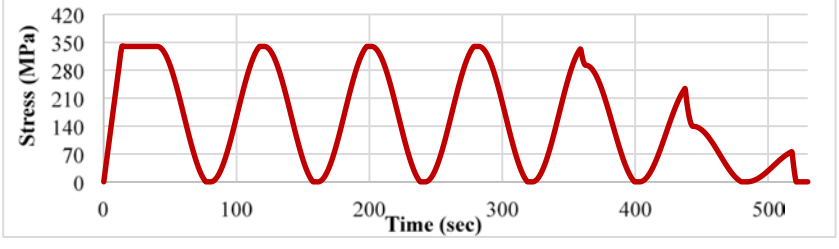


(b) fast-track procedure with $\Delta N = 4$

**Fig. 4.** Cyclic stress levels in the cohesive element with the time (real time) at $f = 0.05$ Hz.

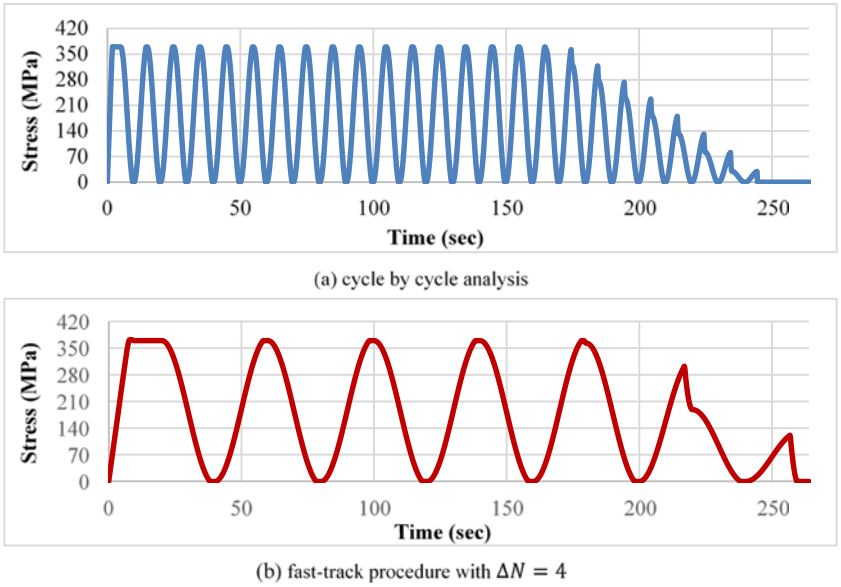


(a) cycle by cycle analysis




(b) fast-track procedure with $\Delta N = 4$

**Fig. 5.** Cyclic stress levels in the cohesive element with the time (real time) at $f = 0.1$ Hz.

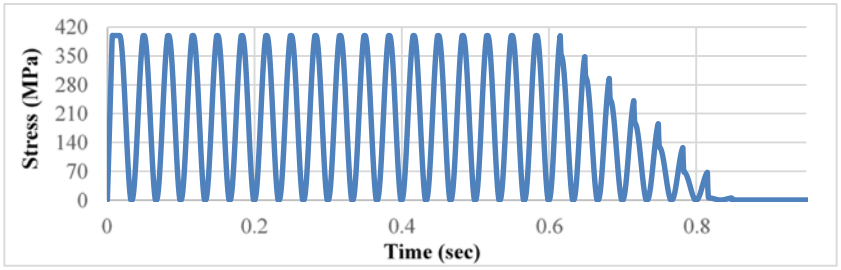


(a) cycle by cycle analysis

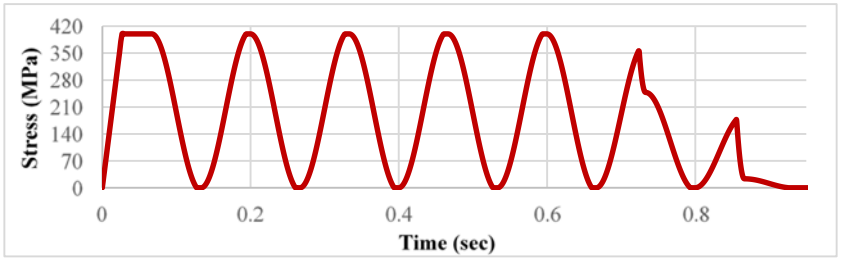


(b) fast-track procedure with $\Delta N = 4$

**Fig. 6.** Cyclic stress levels in the cohesive element with the time (real time) at $f = 30$ Hz.

**Table 3**
Mechanical properties.

| Yield strength (MPa) | | Tensile strength (MPa) | Elongation after fracture (%) | Hardness |
|---|---|---|---|---|
| Rp 0.2% | Rp 0.1% | | | HRB |
| 305 | 340 | 637 | 58 | 85 |

0.05 Hz} were tested with a sigmoidal cyclic load that applied with 10 kN maximum load. During the test the applied displacement was recorded along with the number of cycles at different crack lengths, which enabled the setting of the applied displacement in the FE model. The fatigue specimens containing an edge crack were manufactured to ASTM standard E647. The crack length was measured using a high-resolution camera and analysed using an image processing program. By correlating the number of pixels in the fatigue crack with the number of pixels in a 1 mm mark, the crack length was measured at each side of the specimen and the average is used.

*4.1.3. Experimental results*

The experimental fatigue results demonstrate that the loading frequency has an effect on the crack-growth rate of the austenitic stainless-steel 304 at room temperature. It is clear from Fig. 8 that crack-growth rate decreases and the fatigue life increases with increasing the frequency. This effect is only observed at frequencies lower than around 5 Hz. Although, it is recognised that cracks can grow faster at lower frequencies due to microstructural effects

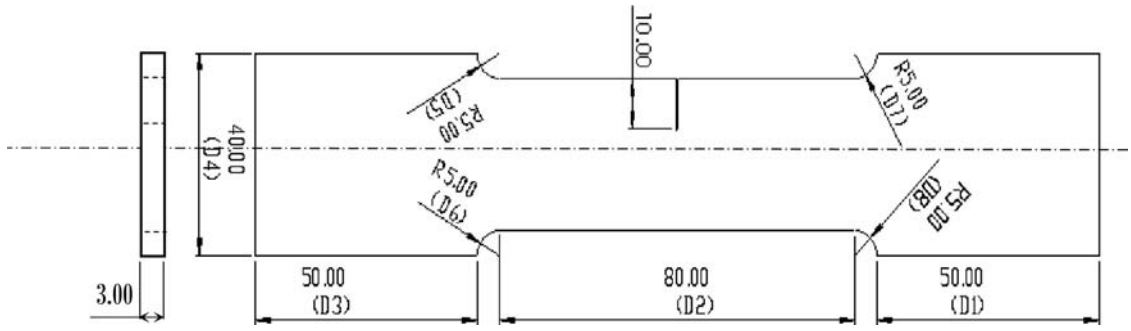


**Fig. 7.** Fatigue test specimen.

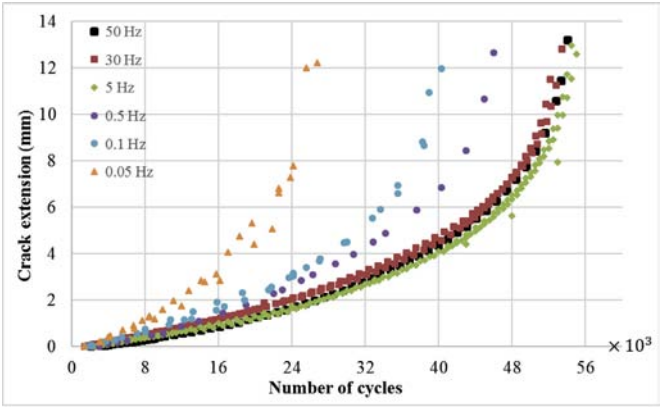


**Fig. 8.** Crack length against number of cycles at different frequencies.

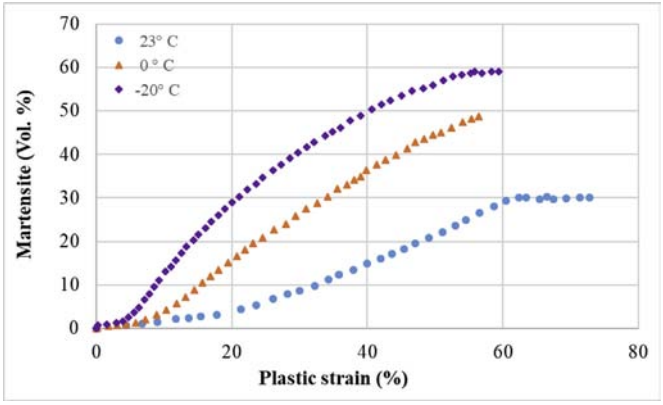


**Fig. 9.** Martensite % as a function of temperature and plastic strain (Müller-Bollenhagen et al., 2010).

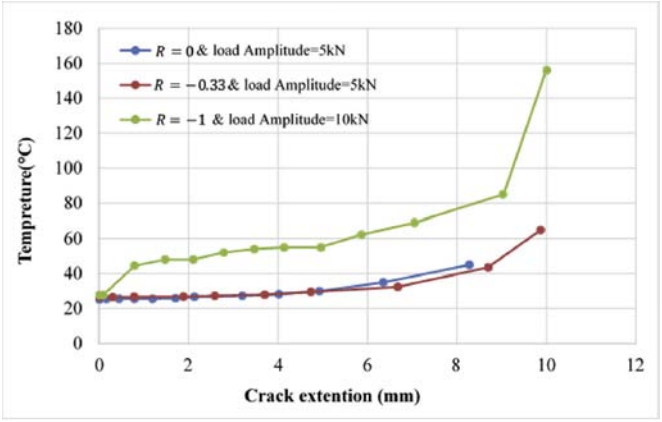


**Fig. 10.** The crack tip temperature as a function of the crack length at $f = 50Hz$.

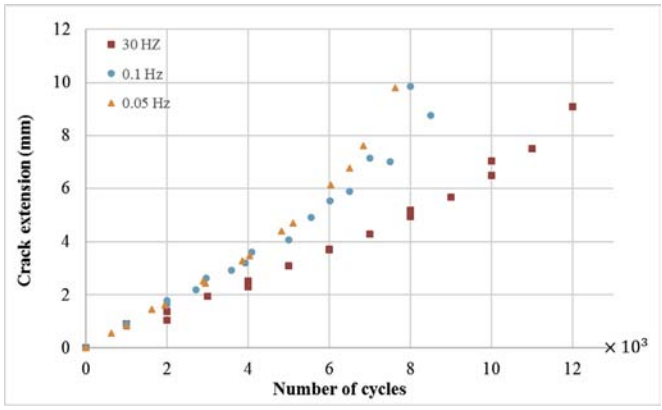


**Fig. 11.** Crack length against number of cycles for $R = -1$.

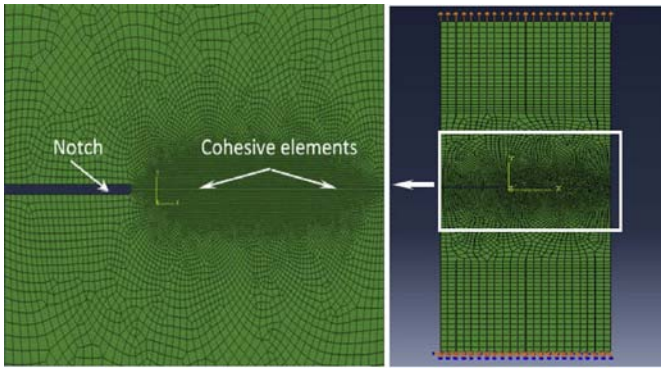


**Fig. 12.** Boundary conditions and loading for FE model.

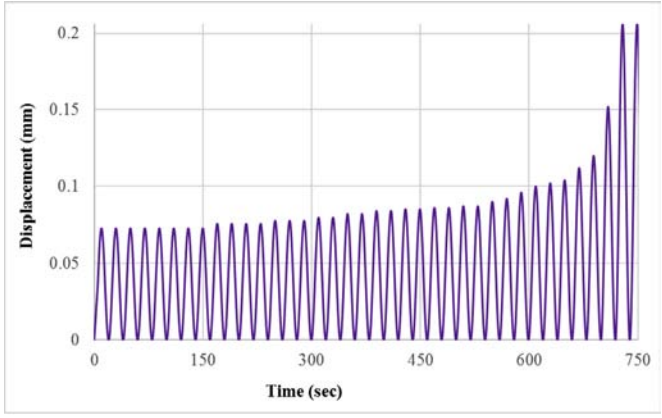


**Fig. 13.** Applied cyclic displacement at $R = 0$, $f = 0.05$Hz & $\Delta N = 800$.

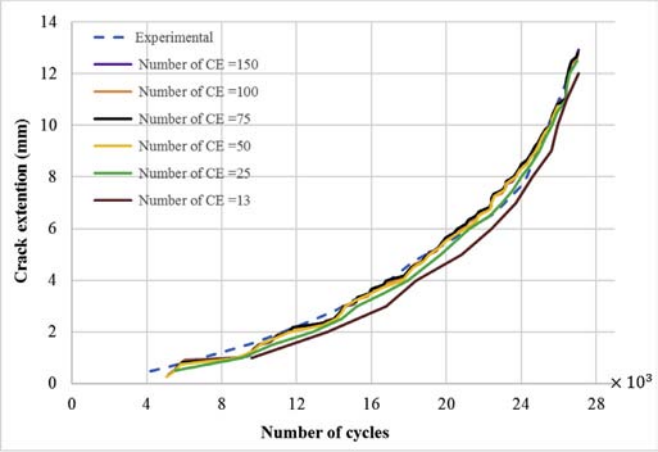


**Fig. 14.** Importance of the number of cohesive elements in the cohesive-zone.

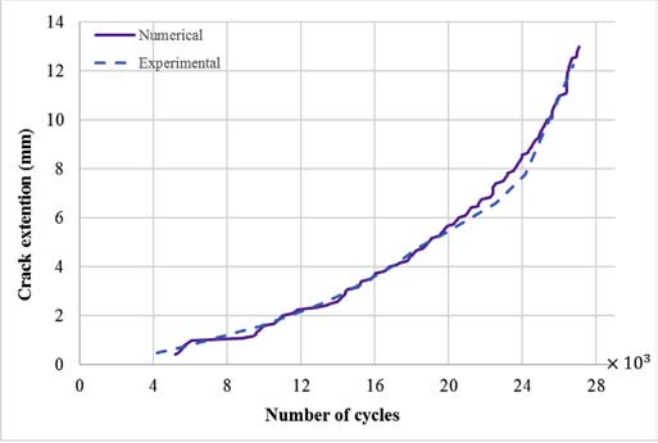


**Fig. 15.** Crack length as function of loading cycles at $R=0$, $f=0.05$Hz & $\Delta N=800$.

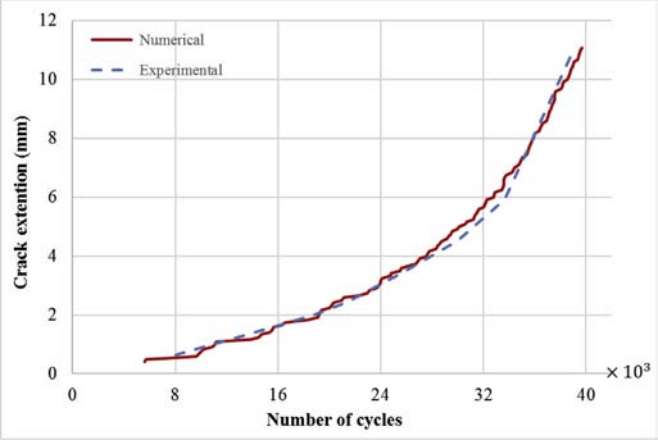


**Fig. 16.** Crack length as function of loading cycles at $R=0$, $f=0.1$Hz & $\Delta N=800$.

or other damage mechanisms such as creep or corrosion (James, 1972; Nikitin and Besel, 2008), creep and corrosion are unlikely to occur in air at room temperature for the material under consideration. It is conjectured therefore that the phase transformation from austenite to martensite is most likely the key factor influencing this behaviour. This transformation depends not only on the plastic strain but also on the temperature see Fig. 9. It is known that for each temperature there is a specific critical plastic strain, below which no phase transformation occurs (Baudry and Pineau, 1977). In addition, it is clear from Fig. 9 that at each temperature there is a saturation limit for the austenite-martensite transformation. For this, reason the frequency effect is not seen above 5 Hz, which means the martensitic content has reached its saturation limit for the specific temperature despite plastic strain increasing. It is observed from Fig. 9 that the maximum percentage of martensite at 23 °C is about 30%. In this study, the temperature at the tip area was 25–28 °C for the steady crack growth period for loading ratio $R=0$ and $R=-0.33$.

The result of this study is in agreement with reference (Müller-Bollenhagen et al., 2010), where no noticeable difference was observed in the fatigue behaviour between frequencies of 90 Hz and 20 KHz. However, it is not in complete agreement with the results of reference (James, 1972), where it is contended that crack growth decreases with increasing frequency as a consequence of self-heating leading to higher temperatures, which is known to inhibit the phase transformation.

It is clear from Fig. 10 that for the case of loading at $R=0$ and $R=-0.33$ the increase in temperature is negligible for a crack length up to 40% of the ligament length and after this length the temperature starts to increase slightly. Although, at $R=-1$ the temperature is higher and increased gradually up to a length of 25% of the ligament length followed by large increase in temperature up to 140 °C at the point of failure, the crack still grows at a faster rate at lower frequency as shown in Fig. 11. The results of this study show that the self-heating of the specimen happens only in the case of reversed loading leading to an increase in the temperature although not sufficient to result in faster crack growth at higher frequency as mentioned in (James, 1972).

### 4.2. Numerical study

#### 4.2.1. Analysis model: geometry and boundary conditions

Shown in Fig. 12 is a finite element model for fatigue specimens used in the experimental trials done in Section 4.1. The model consists of 23,618 plane-stress elements of which 22,988 (type CPS4), 390 (type CPS3), and 240 cohesive elements (type COH2D4). Details on material properties for both the cohesive element and the bulk material elements are presented in Table 1, the numerical analysis was done at six loading frequencies (0.05, 0.1, 0.5, 5, 30, 50). The critical cohesive stress $\sigma_c$ for tests performed at the loading frequency 0.05 Hz is set to be equal to the yield stress of the material. Likewise the value of the parameter $C$ is set by tuning the model with the experimental results at the same loading frequency of 0.05 Hz. The value of $C$ is applied for all the analysis performed at different frequencies yielding good agreement with experimental results and thus provides good supporting evidence for the validity of the approximation in Eq. (16).

Fig. 12 shows the applied boundary conditions for the model, which consists of a uniform cyclic displacement in the y-direction applied at the top surface with the bottom surface is fixed in all directions. A number of stages are involved (see Table 4) in incrementing the applied displacement in order to accurately capture the experimental loading conditions (the displacement values are recorded from the fatigue test). The first stage involves the application of a ramp function to increase the load from zero to $3.65\times10^{-5}$ m. This is followed by stages with a sinusoidal cyclic load at $R=0$, where the number of cycles at each stage is set to ensure a match with the loading conditions incurred in the fatigue experiment. The loading conditions are tabulated in Table 4 and presented for one loading frequency in Fig. 13.

#### 4.2.2. Mesh sensitivity analysis

A mesh sensitivity analysis was preformed to confirm the convergence of the analysis results. It has been found that crack growth-rate predictions show a remarkable insensitivity to mesh,

**Table 4**
Cyclic amplitude with the number of cycles at that amplitude.

| | *f*=0.05 *Hz* | | *f*=0.1 *Hz* | | *f*=0.5 *Hz* | | *f*=0.5, 30 *and* 50 *Hz* | |
|---|---|---|---|---|---|---|---|---|
| | Max $\delta$ (mm) | *N* (cycles) | Max $\delta$ (mm) | *N* (cycles) | Max $\delta$ (mm) | *N* (cycles) | Max $\delta$ (mm) | *N* (cycles) |
| Stage 2 | 0.073 | 6400 | 0.073 | 8000 | 0.073 | 5600 | 0.073 | 8000 |
| Stage 3 | 0.076 | 3200 | 0.0735 | 6400 | 0.0745 | 4800 | 0.0735 | 2400 |
| Stage 4 | 0.078 | 2400 | 0.076 | 4800 | 0.076 | 4800 | 0.074 | 4800 |
| Stage 5 | 0.08 | 1600 | 0.0795 | 3200 | 0.077 | 4000 | 0.075 | 4000 |
| Stage 6 | 0.082 | 1600 | 0.08 | 2400 | 0.078 | 3200 | 0.076 | 3200 |
| Stage 7 | 0.084 | 1600 | 0.083 | 2400 | 0.08 | 3200 | 0.0765 | 3200 |
| Stage 8 | 0.085 | 1600 | 0.085 | 2400 | 0.082 | 2400 | 0.078 | 2400 |
| Stage 9 | 0.86 | 1600 | 0.09 | 2400 | 0.083 | 2400 | 0.079 | 2400 |
| Stage 11 | 0.087 | 1600 | 0.096 | 1600 | 0.085 | 2400 | 0.08 | 2400 |
| Stage 12 | 0.09 | 800 | 0.10 | 1600 | 0.089 | 2400 | 0.081 | 2400 |
| Stage 13 | 0.092 | 800 | 0.102 | 1600 | 0.092 | 2400 | 0.083 | 2400 |
| Stage 14 | 0.096 | 800 | 0.104 | 800 | 0.096 | 2400 | 0.086 | 2400 |
| Stage 15 | 0.10 | 800 | 0.106 | 800 | 0.10 | 2400 | 0.088 | 2400 |
| Stage 16 | 0.102 | 800 | 0.108 | 800 | 0.108 | 2400 | 0.092 | 2400 |
| Stage 17 | 0.104 | 800 | 0.112 | 800 | 0.116 | 2400 | 0.094 | 2400 |
| Stage 18 | 0.112 | 800 | 0.116 | 800 | 0.132 | 800 | 0.098 | 1600 |
| Stage 19 | 0.12 | 800 | 0.12 | 800 | 0.144 | 800 | 0.102 | 1600 |
| Stage 14 | 0.152 | 800 | 0.124 | 800 | 0.176 | 800 | 0.108 | 1600 |
| Stage 16 | 0.206 | until failure | 0.13 | 800 | 0.206 | until failure | 0.12 | 1600 |
| | | | 0.206 | until failure | | | 0.132 | 800 |
| | | | | | | | 0.148 | 800 |
| | | | | | | | 0.206 | until failure |

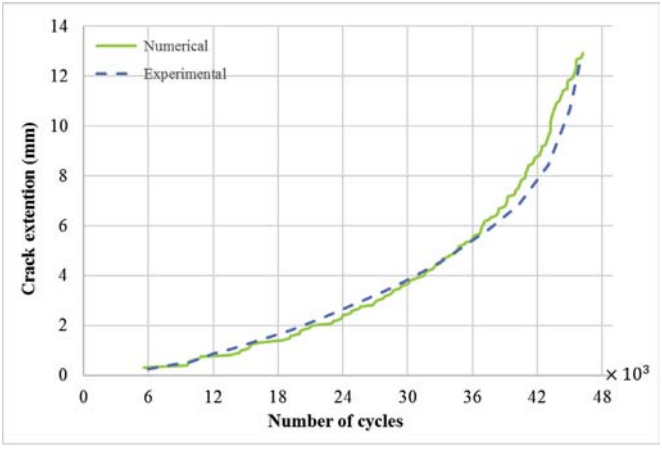


**Fig. 17.** Crack length as function of loading cycles at $R$=0, $f$=0.5Hz & $\Delta N$800.

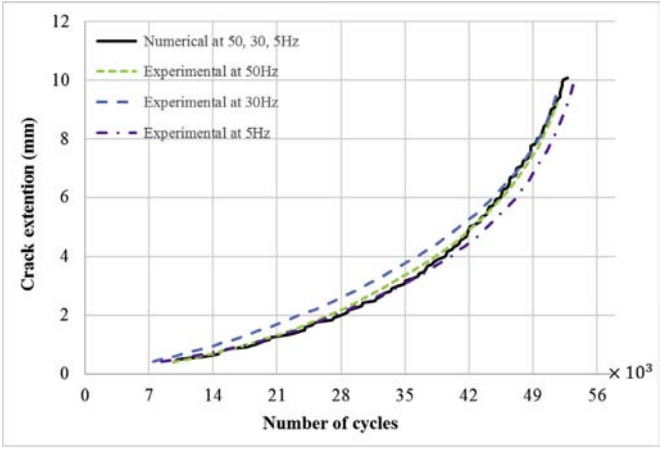


**Fig. 18.** Crack length as a function of loading cycles at $R$=0, $f$=5, 30 and 50Hz & $\Delta N$800.

i.e. increasing the overall number of bulk and cohesive elements has little impact on predictions. Greatest mesh sensitivity however is displayed in the cohesive zone and a reasonable estimate for the size of this zone is obtainable from the relationship:

$$l_{coh} = \frac{E}{2\pi}\frac{G_{Ic}}{\sigma_c^2} \tag{17}$$

which for the loading considered provides a value of 12.5 mm.

The effect of varying the number of cohesive elements used in the cohesive zone is illustrated in Fig. 14. The results confirm that reasonable predictions are possible with only a small number of elements in the cohesive-zone and convergence is obtained when the number of cohesive elements is higher than 50.

### 4.2.3. Numerical results

The cohesive zone model introduced in Section 2 is used to simulate the fatigue tests performed in Section 4.1 and the numerical results confirm that the new cohesive model can predict crack growth behaviour at different loading frequencies with good accuracy and with a significant reduction in the required CPU time. The advantages of the new frequency-dependent CZM over the available models in the literature (e.g. (De-Andrés et al., 1999; Towashiraporn et al., 2005; Koutsourelakis et al., 2006; B.L. V Bak et al., 2014)) are the ability to capture the frequency effect and its simplicity. It does not require the formation of a relationship to link the damage to the number of cycles as in previous work. Another advantage of the model is that it can be applied to both low and high-cycle fatigue analysis, since the number of cycles in the load envelope $\Delta N$ that used for the fast-track procedure is automatically set according to the problem under consideration.

The numerical predicted curves for crack growth with the number of cycles along with experimental curves for different loading frequencies are shown in Figs. 15 to 18. Fig. 15 presents the result at loading frequency $f = 0.05$ Hz which is used to tune the cohesive parameters (i.e. $f_o$ and $C$) for the new model since $\sigma_{(f)}^{c_{rate}}$ for this loading frequency set to be equal to the material yield stress at 0.1% strain and $\delta_c$ set to be equal to the crack tip opening displacement measured on a CT specimen. By using these cohesive properties, the fixed parameter $C$ was determined first by tuning the analysis result with the experimental data at 0.05 Hz. The value of critical stress limit $\sigma_{(limit)}^{c}$ is then evaluated by tuning with the

**Table 5**
Percentage difference in predicted and experimentally determined crack lengths.

| $N$ (cycles) | $f$=0.05 Hz | | $f$=0.1 Hz | | $f$=0.5 Hz | | $f$=50 Hz | |
|---|---|---|---|---|---|---|---|---|
| | $a$ (mm) | Error % | $a$ (mm) | Error % | $a$ (mm) | Error % | $a$ (mm) | Error % |
| 8000 | 0.98 | −19.30 | 0.50 | −19.80 | 0.38 | −6.62 | 0.30 | 7.64 |
| 12,000 | 2.18 | −0.40 | 1.04 | −7.60 | 0.79 | −10.00 | 0.56 | −2.15 |
| 17,000 | 3.96 | −1.94 | 1.77 | 0.09 | 1.36 | −10.00 | 0.89 | −4.40 |
| 20,000 | 5.586 | 2.20 | 2.25 | −6.25 | 1.75 | −10.00 | 1.15 | −5.66 |
| 24,000 | 7.75 | 0.96 | 3.10 | 2.10 | 2.42 | −8.80 | 1.50 | −9.58 |
| 28,000 | | | 4.19 | 4.24 | 3.25 | −4.40 | 2.00 | −8.51 |
| 32,000 | | | 5.60 | −5.86 | 4.25 | −1.16 | 2.60 | −7.80 |
| 36,000 | | | 8.17 | 0.27 | 5.50 | −1.44 | 3.29 | −7.00 |
| 40,000 | | | | | 7.40 | 8.82 | 4.22 | −3.00 |
| 44,000 | | | | | | | 5.50 | 0.60 |
| 48,000 | | | | | | | 7.25 | 4.10 |
| 52,000 | | | | | | | 9.50 | −1.32 |

experimental result at loading frequency (50 Hz). Finally, the value of the base frequency $f_o$ was found using Eq. (16) by applying the value of $\sigma^c_{(limit)}$ and the cohesive parameters at 0.05 Hz. Predictions obtained with these settings when compared with data at other frequencies (i.e. 0.1, 0.5, 5 and 30 Hz) provide good support for the form of Eq. (16) and the new model. The predicted and experimentally obtained crack growth at loading frequencies of 0.1 Hz and 0.5 Hz are shown in Figs. 16 and 17, respectively, with the results at 5, 30, and 50 Hz shown in Fig. 18. It is clear from the results that the predicted growth rate by the new model at different loading frequencies is in good agreement with the experimental results. The percentage of error in the estimated crack length [(estimated length-measured length)/measured length) × 100%] is shown in Table 5, where the minus sign signifies that the model is under estimating the crack length. From the results in Table 5, it is clear that the predicted crack length matches the measured length to an acceptable level of accuracy.

## 5. Conclusion

Presented in the paper is a new frequency-dependent trapezoidal cohesive-zone model with fast-track facility that can be used for low and high-cycle fatigue simulation. The following conclusions can be drawn from the results presented:

- Loading frequency has an effect on the crack-growth in austenitic stainless-steel 304 at room temperature.
- Fatigue cracks grow faster at lower frequency and slower at higher frequency in austenitic stainless-steel 304 as a result of a likely increase in martensitic content.
- Crack growth rates are similar for frequencies above 5 Hz.
- The rate-dependent critical stress increases with loading frequency up to 5 Hz and takes up a nearly constant value at frequencies higher than 5 Hz.
- The new frequency-dependent CZM model has been shown to give an acceptable prediction with a significant reduction in the computational time of the order of $\Delta N^{-1}$.
- The number of elements in the cohesive-zone has a minor effect on the crack growth prediction.
- A limitation of the model is that it does consider the effect of R-ratio, and this should be considered in future works.

## Acknowledgements

The authors would like to acknowledge the Higher Committee for Education Development in Iraq for funding Mr Sarmed Salih.

## Reference

ABAQUS, 2013. ABAQUS 6.13 User Guide. Dassault Systèmes Simulia Corp, USA.
Bak, B.L.V., Sarrado, C., Turon, A., Costa, J., 2014a. Delamination under fatigue loads in composite laminates: a review on the observed phenomenology and computational methods. Appl. Mech. Rev. 66 (6).
Bak, B.L.V, Lindgaard, E., Lund, E., Turon, A., 2014b. Performance of cohesive zone models for fatigue driven delaminations. In: 11th World Congress on Computational Mechanics (WCCM XI), pp. 1–2.
Baudry, G., Pineau, A., 1977. Influence of strain-induced martensitic transformation on the low-cycle fatigue behavior of a stainless steel. Mater. Sci. Eng. 28 (2), 229–242.
Beaurepaire, P., Schuëller, G.I., 2011. Modeling of the variability of fatigue crack growth using cohesive zone elements. Eng. Fract. Mech. 78 (Aug (12)), 2399–2413.
Colin, J., Fatemi, A., Taheri, S., 2010. Fatigue behavior of stainless steel 304 L including strain hardening, prestraining, and mean stress effects. J. Eng. Mater. Technol. 132 (2), 21008.
De-Andrés, A., Pérez, J., Ortiz, M., 1999. Elastoplastic finite element analysis of three--dimensional fatigue crack growth in aluminum shafts subjected to axial loading. Int. J. Solids Struct. 36 (15), 2231–2258.
Ganesh Sundara Ranan, S., Padmanabhan, K.A., 1995. A comparison of the room-temperature behaviour of AISI 304LN stainless steel and Nimonic 90 under strain cycling. Int. J. Fatigue 17 (May (4)), 271–277.
James, L.A., 1972. The effect of frequency upon the fatigue-crack growth of Type 304 stainless steel at 1000°F. In: Stress Analysis and Growth of Cracks: Proceedings of the 1971 National Symposium on Fracture Mechanics: Part 1, pp. 218–229.
Koutsourelakis, P.S., Kuntiyawichai, K., Schuëller, G.I., 2006. Effect of material uncertainties on fatigue life calculations of aircraft fuselages: A cohesive element model. Eng. Fract. Mech. 73 (9), 1202–1219.
Lebedev, A.A., Kosarchuk, V.V., 2000. Influence of phase transformations on the mechanical properties of austenitic stainless steels. Int. J. Plast. 16 (7–8), 749–767.
Müller-Bollenhagen, C., Zimmermann, M., Christ, H.-J., 2010. Very high cycle fatigue behaviour of austenitic stainless steel and the effect of strain-induced martensite. Int. J. Fatigue 32 (6), 936–942.
Nguyen, O., Repetto, E., 2001. A cohesive model of fatigue crack growth. Int. J. Fract. 110, 351–369.
Nikitin, I., Besel, M., 2008. Effect of low-frequency on fatigue behaviour of austenitic steel AISI 304 at room temperature and 25 °C. Int. J. Fatigue 30 (10–11), 2044–2049.
Roe, K.L., Siegmund, T., 2003. An irreversible cohesive zone model for interface fatigue crack growth simulation. Eng. Fract. Mech. 70 (Jan (2)), 209–232.
Salih, S., Davey, K., Z. Z., 2017. Frequency-dependent cohesive zone models for fatigue. 6th International Conference on Fracture Fatigue and Wear.
Salih, S., Davey, K., Zou, Z., 2016. Rate-dependent elastic and elasto-plastic cohesive zone models for dynamic crack propagation. Int. J. Solids Struct. 0, 1–21.
S. Salih, K. Davey, and Z. Zou, "A computationally efficient cohesive-zone model for fatigue," *Submitt. to Fatigue Fract. Enginering Mater. Struct.*
Scheider, I., Schödel, M., Brocks, W., Schönfeld, W., 2006. Crack propagation analyses with CTOA and cohesive model: comparison and experimental validation. Eng. Fract. Mech. 73 (Jan (2)), 252–263.
Towashiraporn, P., Subbarayan, G., Desai, C.S., 2005. A hybrid model for computationally efficient fatigue fracture simulations at microelectronic assembly interfaces. Int. J. Solids Struct. 42 (15), 4468–4483.
Ural, A., Krishnan, V.R., Papoulia, K.D., 2009. A cohesive zone model for fatigue crack growth allowing for crack retardation. Int. J. Solids Struct. 46 (Jun (11–12)), 2453–2462.
Yang, B., Mall, S., Ravi-Chandar, K., 2001. A cohesive zone model for fatigue crack growth in quasibrittle materials. Int. J. Solids Struct. 38 (May (22–23)), 3927–3944.
Ye, D., Matsuoka, S., Nagashima, N., Suzuki, N., 2006. The low-cycle fatigue, deformation and final fracture behaviour of an austenitic stainless steel. Mater. Sci. Eng. A. 415 (1–2), 104–117.